Semi-automated registration-based anatomical labelling, voxel based morphometry and cortical thickness mapping of the mouse brain

Research Article

Semi-automated registration-based anatomical labelling, voxel based morphometry and cortical thickness mapping of the mouse brain

Marco Pagani[1,2¶*], Mario Damiano[1¶], Alberto Galbusera[1], Sotirios A Tsaftaris[3&], Alessandro Gozzi[1&*]

[1] Center for Neuroscience and Cognitive Systems, Istituto Italiano di Tecnologia, Rovereto, Italy.
[2] Centro Interdipartimentale Mente/Cervello (CIMeC) - University of Trento, Rovereto, Italy.
[3] IMT Institute for Advanced Studies, Lucca, Italy.

[¶] *The two authors equally contributed to this work*
[&] *The two authors share senior authorship*

[*]**Corresponding Authors:**

e-mail: alessandro.gozzi@iit.it
e-mail: marco.pagani@iit.it

Highlights

- We describe registration-based methods for mouse brain morphoanatomical imaging.
- Detailed workflows for anatomical labelling, voxel based morphometry and cortical thickness are reported.
- The same preprocessing can be applied to map multiple complementary anatomical readouts.
- The present work may help to promote the use of rodent morphoanatomical imaging.

Abstract

Background

Morphoanatomical MRI methods have recently begun to be applied in the mouse. However, substantial differences in the anatomical organisation of human and rodent brain prevent a straightforward extension of clinical neuroimaging tools to mouse brain imaging. As a result, the vast majority of the published approaches rely on tailored routines that address single morphoanatomical readouts and typically lack a sufficiently-detailed description of the complex workflow required to process images and quantify structural alterations.

New method

Here we provide a detailed description of semi-automated registration-based procedures for voxel based morphometry, cortical thickness estimation and automated anatomical labelling of the mouse brain. The approach relies on the sequential use of advanced image processing tools offered by ANTs, a flexible open source toolkit freely available to the scientific community.

Results

To illustrate our procedures, we described their application to quantify morphological alterations in socially-impaired BTBR mice with respect to normosocial C57BL/6J controls, a comparison recently described by us and other research groups. We show that the approach can reliably detect both focal and large-scale gray matter alterations using complementary readouts.

Comparison with existing methods

No detailed operational workflows for mouse imaging are available for direct comparison with our methods. However, empirical assessment of the mapped inter-strain differences is in good agreement with the findings of other groups using analogous approaches.

Conclusion

The detailed operational workflows described here are expected to help the implementation of rodent morphoanatomical methods by non-expert users, and ultimately promote the use of these tools across the preclinical neuroimaging community.

Keywords

Voxel Based Morphometry; Cortical Thickness; Anatomical Labelling; Mouse Brain; MRI.

1. Introduction

A deep understanding of the genetic, physiological and anatomical underpinnings of brain disease is essential for the development of improved therapies. A milestone towards this goal is the generation of genetically modified mouse lines that recapitulate targeted genetic mutations in experimentally controlled studies. Genetically modified mouse lines permit to relate genetic mutations to clinically relevant endophenotypes without the complexity of genetic heterogeneity and the uncontrolled impact of gene-gene and gene-environment interactions in adult human populations (Nestler and Hyman, 2010).

Magnetic resonance imaging (MRI) methods offer a privileged point of view to study genetically altered mouse models of neuropsychiatric disorders in many respects. First, the use of comparable imaging readouts in men and mice permits a cross-species comparison of brain endophenotypes of translational relevance, thus enhancing the transfer of information from and to the clinic. At the same time, MRI readouts can also be employed to assess the extent to which mouse models of central nervous system pathology replicate neuroimaging findings observed in clinical populations, informing preclinical researchers on the translational validity of these models. Moreover, high resolution morphometric MRI, achievable at ultra-high field strength or in *ex vivo* formalin-fixed samples (Lerch et al., 2012; Tucci et al., 2014) can be employed to obtain a fine-grain assessment of structural brain alterations that could serve as a convenient surrogate for labour intensive manual morphometric measurements in *ex vivo* brain slice preparations, with the additional advantage of being non-invasive and multi-dimensional.

Structural MRI based imaging methods - such as voxel based morphometry (VBM) of gray matter (GM), cortical thickness mapping and anatomical labelling - have been widely employed to study brain morphology in human populations (Mueller et al., 2012). The application of analogous readouts to map genetically determined brain alterations in transgenic mouse lines has been recently proposed, an effort collectively referred to as MRI phenotyping (Borg and Chereul, 2008; Johnson et al., 2007; Lerch et al., 2011a). Recent improvements in MRI sequences and hardware, together with the development of fixation protocols for *ex vivo* imaging of stained brain specimens (Lerch et al., 2012), have made it possible the acquisition of artefact-free and high resolution – with a voxel size less than 80 μm – mouse brain volumes even at relatively low magnetic field strengths. This efforts have resulted in the publication of several examples or the application of morphoanatomical imaging to transgenic mouse models (Lerch et

al., 2008; Sawiak et al., 2009; Xie et al., 2010; Yushkevich et al., 2006).

The development of standardised preprocessing and analytical pipelines for human imaging data, and their implementation in popular software toolkits such as such as FMRIB Software Library (FSL) (Jenkinson et al., 2012), Statistical Parametric Mapping (SPM) (Friston et al., 1994) and Advanced Normalization Tools (ANTs) (Avants et al., 2009), have been instrumental to the widespread use of MRI in human brain research. However, substantial differences in the dimensions and anatomical organisation of the human and rodent brain prevent a straightforward extension of these tools to morphoanatomical mouse brain mapping. As a result, several research groups have developed tailored procedures for the preprocessing and analyses of morphoanatomical brain MRI readouts in mouse models (Badea et al., 2012; Borg and Chereul, 2008; Delatour et al., 2006; Johnson et al., 2007; Lee et al., 2010; Lerch et al., 2011a; Nieman et al., 2005; Sawiak et al., 2009; Sawiak et al., 2013). However, the vast majority of the published approaches typically address single morphoanatomical readouts (e.g., VBM *or* anatomical labelling *or* cortical thickness), and lack a detailed description of the complex workflow and computational parameters required to process, analyse and quantify structural MRI alterations, thus complicating the implementation of these procedures by non-expert users.

To begin to address these issues, here we provide a detailed methodological description of a semi-automated operational workflow for VBM, cortical thickness estimation and automated anatomical mapping of the mouse brain. To simplify and streamline operations, we based image processing mainly on ANTs (Avants et al., 2009), a flexible and powerful open source toolkit freely available to the scientific community. Importantly, our approach has been recently applied by our research group to map fine-grain brain anatomy alterations in different mutant mouse lines (Dodero et al., 2013; Lassi et al., 2015; Minervini et al., 2014; Sannino et al., 2014; Tucci et al., 2014) and to describe large-scale networks of anatomical covariance between gray matter regions in wild-type mice (Pagani et al., 2016), with excellent agreement between MRI and manual morphometric measurements (Sannino et al., 2014), exhibiting corresponding morphoanatomical features in mice and reference clinical populations (Cutuli et al., 2016; Tucci et al., 2014). Below, we provide a detailed description of our procedural workflow and show its capabilities by describing its application to quantify morphological alterations in socially-impaired BTBR T+Itpr3tf/J mice with respect to normo social C57BL/6J controls (Dodero et al., 2013; Squillace et al., 2014), a comparison that has been recently described by our research

group (Dodero et al., 2015) and others (Ellegood et al., 2013), thus permitting an empirical cross-laboratory assessment of the validity of our findings.

2. Materials and Methods

2.1. Ethical statement

All *in vivo* studies were conducted in accordance with the Italian law - D.L. n° 116, 1992, Ministero della Sanità, Roma - and following the recommendations in the Guide for the Care and Use of Laboratory Animals of the National Institutes of Health. The animal research protocol was approved by the Animal Care Committee of the Istituto Italiano di Tecnologia (Permit Date 07-2012). All surgical procedures were performed under deep anaesthesia.

2.2. Sample Preparation and MR acquisition

High-resolution morphoanatomical T2-weighted MR imaging of mouse brains was performed in paraformaldehyde (4% PFA; 100 ml, Sigma, Milan) fixed specimens, a procedure employed to obtain high-resolution images with negligible confounding contributions from physiological or motion artefacts (Cahill et al., 2012). Sample preparation and MRI acquisition of BTBR T+Itpr3tf/J (BTBR) and C57BL/6J (B6) mice has been recently described in previous work (Dodero et al., 2013; Sforazzini et al., 2014a; Sforazzini et al., 2014b) and is briefly summarised here. Male BTBR (N=9, 15-26 weeks old) and age-matched control B6 (N=9) mice were deeply anaesthetized with an intraperitoneal Avertin injection (375 mg/Kg, Sigma, Milan) and their brains were perfused *in situ* via cardiac perfusion. The perfusion was performed with phosphate buffered saline followed by paraformaldehyde (4% PFA; 100 ml). Both perfusion solutions were added with a Gadolinium chelate (Prohance, Bracco, Milan) at a concentration of 10 and 5 mM, respectively, to shorten longitudinal relaxation times (Lerch et al., 2012).

A multi-channel 7.0 Tesla MRI scanner (Bruker Biospin, Milan) was used to acquire anatomical images of the brain, using a 72 mm birdcage transmit coil, a custom-built saddle-shaped solenoid coil for signal reception, and the following imaging parameters: 3D RARE spin-echo sequence, TR=550 ms, TE=33 ms, RARE factor=8, echo spacing 11ms, matrix size of 192x 170x170 and voxel size of 0.09 mm (isotropic), with a total acquisition time of 4 hrs and 25 mins.

2.3. Image preprocessing and analysis

A detailed description of the image processing workflow employed to create a study based template, to estimate cortical thickness, and to perform automated anatomical labelling and VBM is reported below for structural images acquired at 7 Tesla. We refer to our approach as "registration-based" as several preprocessing and estimation steps (e.g., cortical thickness) are executed via a combination of affine and symmetric diffeomorphic transformations as implemented in *antsRegistration* command (Avants et al., 2014). The tool entails the application of affine registration with twelve degrees of freedom to coarsely normalise the overall shape of a source image to a reference image. Afterwards, a non-linear transformation is applied to create a differentiable and invertible diffeomorphic map which locally aligns source and reference image by adjusting for local inter-individual morphological differences.

Flowcharts are provided as a visual reference to guide the description of each computational step, where light grey shading denotes image inputs, dark grey shading denotes the final output and computational processes are outlined in the form of rectangular boxes. All the computational steps have been carried out using tools and algorithms implemented within the ANTs toolkit (version 1.9 http://sourceforge.net/projects/advants/) and employed to process 3D RARE morphoanatomical images acquired at 7 Tesla with the image sequence parameters described above. The parameter employed for the preprocessing steps were optimized in pilot assessments using both empirical (e.g. segmentation) and quantitative approaches (e.g. registration).

2.3.1. Image preprocessing

Basic image preprocessing includes bias field correction and skull stripping (Figure 1). As a first step, all the images are corrected for intensity non-uniformity using *N3BiasFieldCorrection,* an automated algorithm implemented within the ANTs toolkit using 50 fitting levels. This step reduces bias field signal related to the reception profile of MRI receive coils, a low frequency amplitude modulation of the signal that produces regional variation in voxel intensity as a function of coil proximity. The correction of this bias is an important pre-requisite for subsequent intensity based MR image processing, such as tissue segmentation.

Skull stripping is required to remove extra brain tissue, thus crucially improving the

accuracy of subject-to-template registration. In order to automate skull-stripping and avoid tedious and error-prone manual segmentation, an automatic registration-based approach to skull stripping was devised. This is carried out by registering the bias adjusted MRI volumes to a skull stripped reference image using an affine and diffeomorphic registration algorithm. The skull stripped reference image should ideally be chosen from the study population or from comparable experiments of the same laboratory. A companion brain binary mask of the reference image can be segmented manually. While potentially labour intensive in high resolution brain images, this process can be performed only once, and it is instrumental to automating skull stripping for all the subsequent subjects and analyses. After the registration, the diffeomorphic map is applied to non-linearly transform the brain mask of the reference image into the subjects' space using *WarpImageMultiTransform*. The subject's brain mask is then applied to each original subject image to obtain skull stripping. An additional bias correction is subsequently performed on the skull stripped subject image to achieve a more accurate estimation of the bias field, devoid of the contribution of non-brain related protrusions.

An illustrative example of the advantage of performing two independent bias corrections, (before and after skull stripping, respectively) is reported in Figure 2. Even though the first step does not flawlessly compensate for signal inhomogeneity in all brain regions (i.e. the ventral areas of the brain and in the ventricles), its use provides a first normalization of signal intensity that results in an improved the accuracy of registration based estimation of brain mask, and the removal of brain extra tissue. After this skull stripping step, the bias field of the original subject image is re-estimated, leading to a more accurate bias correction. The results of this first-pass skull stripping are typically visually inspected for imperfections, usually present in a minority of subjects, which can be easily manually corrected, for example using the brushtool of ITKsnap (Yushkevich et al., 2006). For each subject, the result of preprocessing is a skull stripped and bias corrected brain image, exhibiting uniform contrast within the same tissue class, and its binary mask.

2.3.2. Study based template

A critical element in our approach is the construction of a study based template to establish a common reference space for all the subsequent analyses. In cross-sectional mouse studies, the most adopted experimental designs for mouse phenotyping with transgenic lines, this

involves the creation of an average template from a reference population, typically the control subjects (B6 in this study). This leads to the generation of a template recapitulating neuroanatomical features of "healthy" or reference population, avoiding the combination of conflicting morphoanatomical traits which could affect subsequent computational steps (e.g. segmentation). For example, the use of both normo-callosal B6 and acallosal BTBR mice for template creation would result in a chimeric image exhibiting a blurred and hypo-intense corpus callosum, a feature that could negatively affect the quality of subsequent segmentation priors. The creation of different templates for different studies can help minimizing confounding effects related, for instance, to perfusion, age, sex and brain sizes.

Study-based template creation was implemented via the use of the *buildtemplateparallel* script available within the ANTs toolkit (Avants et al., 2010b). This script entails an automated and iterative intensity-based registration approach to automatically create a study based template using a predefined list of subjects (Kovacevic et al., 2005). A representative subject is selected as initial reference and each subject is linearly registered to the reference subject using an affine transformation. After intensity averaging all registered images to obtain a first linear group average, an iterative five-generation multi-scale non-linear alignment process is performed using a *Greedy Syn* diffeomorphic registration algorithm (Avants et al., 2008) with a maximum of 120 iterations for each step. This process entails an initial diffeomorphic registration of each subject to the reference linear group average to obtain individuals' warps using cross correlation as similarity metric. These warps are then averaged and applied to the template to update its shape and conform it to the population shape. The process is iteratively repeated four more times, by using as reference the warped template from the previous iteration. The final outcome is an average template volume exhibiting clear structural boundaries, incorporating fine grain neuroanatomical descriptions of the reference population, and reduced intensity variation.

2.3.3. Anatomical labelling

The assessment of subtle anatomical differences in gross morphology via manual delineation of brain structures is a laborious and time consuming task that may introduce intra- and inter-observer bias (Badea et al., 2012). The procedures described here allows for volumetric estimation via anatomical labelling, a procedure whereby brain regions can be labelled and classified depending on their anatomical location. The process employed in our workflow relies

on the availability of preprocessed images, a study-based template and two neuroanatomical labelled reference MRI atlases for cortical (Ullmann et al., 2013) and subcortical (Dorr et al., 2008) areas, respectively. The output of automated anatomical labelling is a fine-grained projection of a given anatomical label in the subject's coordinate space. The anatomical labels thus registered can be used both to measure the volume of anatomical regions of interest for cross-strain statistical comparison, or as intermediate input for further analyses, such as cortical thickness estimation (Figure 3).

The volume of specific anatomical regions in individual subjects is computed using a template based anatomical labelling strategy (Avants et al., 2010b). As previously reported in the literature, the propagation of labels from the anatomical labelled atlas to the subject space is more accurate when performed via the study based template to minimize variation due to registration errors (Jia et al., 2011). To this purpose, a composition of affine and diffeomorphic (SyN) registration between the reference neuroanatomical atlas and the study based template is performed to project the anatomical labels in the coordinate system of the study based template (Avants et al., 2009) For the anatomical images and RARE sequence used in this study we adopted cross correlation as similarity metric, with a window radius of 5 and a gradient step length of 0.25. The optimisation was performed over four resolutions for both transformations with a maximum of 100 iterations for the coarse levels and 10 at the full resolution. A simple propagation of the neuroanatomical labels mapped in the study-based template space to the subjects' space can then be achieved via the registration of each subject to the study based template and the subsequent propagation of the labels to each subject. The efficiency of the registration procedures can evaluated using the Dice coefficient (*DiceAndMinDistSum* command from *ImageMath)*, which quantifies the overlap between a manually defined label and the same label resulting from our automated labelling, in the subject space (Dice, 1945). Label volumes can then be easily computed using tools included in several MRI software packages (e.g. *LabelStats* command from *ImageMath*, or FSL's *fslstats*).

2.3.4. VBM

VBM is a whole-brain technique for characterizing regional brain volume and differences in tissue concentration, in particular GM, across subjects. In our procedure, it consists of five main steps (Figure 4).

First, a study based template is created using brain anatomical images from reference population described above. Second, the original images of the two groups of subjects are registered to the study based template via the same affine and diffeomorphic mapping used for anatomical labelling. Third, spatially normalized images are segmented using a Markov Random Field model, implemented by the *Atropos* command of the ANTs toolkit (Avants et al., 2011). To classify tissues we applied a smoothing factor of 0.0125, a radius of 1 and the maximum number of iterations was set at 10. The separation of GM (i.e. the readout of interest) from white matter (WM) and cerebrospinal fluid (CSF) is improved by initializing the process with the study based template, previously segmented using standard k-means clustering included in the *Atropos* command. (Figure 5, B-C). This step is especially critical and it is therefore here described in greater detail. In pilot work, we explored the number of tissue classes leading to optimal separation of GM from non-GM components (WM plus CSF). A canonical three-class segmentation of *ex vivo* mouse brain using *Atropos* results in inefficient GM/WM segmentation, leading to an overestimation of WM fraction at the expense of GM (Figure S1). The use of six independent classes results in three GM clusters that can be merged to provide a final accurate GM map (Fig. 5). A similar approach has been employed by other investigators (e.g. (Li et al., 2009)). Our segmentation procedure results in a two-voxel layer on the outmost edge of the cortex which is labelled as "non gray matter" and, as such, is not included in subsequent analysis. These voxels are characterised by low or very-low signal intensity and reflect a combination of partial volume effects between gray matter and non MRI visible skull signal, and possibly also small inaccuracies due to registrations. In our workflow, these "low confidence" gray matter voxels are discarded to improve the robustness of subsequent voxelwise statistical mapping.

In our procedure, the quality of segmentation is assessed empirically by comparing individual and merged tissue classes with the anatomical distribution of known high-density WM structures such as the corpus callosum, anterior and posterior commissures, as seen in the study based template (Figure 5). These structures are easily identifiable and their extension can be compared with their segmented counterparts. Future developments of our initial workflow could employ quantitative approaches to estimate goodness of cluster separation (Chou et al., 2004; Wu and Yang, 2005), although operator dependent assessments of tissue class separations are ultimately warranted to ensure biologically meaningful results.

It should be noted that the segmentation procedure employed in our work does not always lead to a clear separation of WM and CSF, at least on brain volumes acquired *ex vivo*. Besides differences in the anatomical organization of the mouse brain and image contrast in the PFA perfused brain (Cahill et al., 2012), a contributing reason for this is the occurrence of CSF loss from the brain in a large proportion (ca. 70%) of the subjects as a consequence of the *ex vivo* fixation procedure, leading to the presence of signal voids in ventricular space. These low signal-intensity intra-ventricular foci are typically classified as WM, leading to mixed or incomplete separation between these two brain components. Such incomplete separation however does not limit the validity of our approach, because both CSF and WM (even if separate) would invariably end up being discarded from subsequent GM-based analyses (i.e. VBM and cortical thickness).
After tissue segmentation, the Jacobian determinants of the deformation are calculated with *ANTSJacobian* command of the ANTs toolkit and used to modulate the GM probability maps calculated during the segmentation step. This step permits the analysis of GM probability maps in terms of local anatomical variation instead of tissue density (Ashburner and Friston, 2000). Jacobian determinants can be also normalized by the total intracranial volume to further eliminate overall brain volume variations and calculate relative GM volumes. Fifth, the resulting modulated GM probability maps are smoothed using a Gaussian kernel with a sigma of three voxel width (FWHM=0.64mm) and employed for voxel-wise statistical comparison.

2.3.5. Cortical Thickness

The proposed registration-based cortical thickness *DiReCT* estimation approach (Figure 3) is a voxelwise computational approach based on the method presented by Das and colleagues (Das et al., 2009) and relies on the *KellyKapowsky* command within ANTs toolkit. The method provides cortical thickness measurements at the voxel level using cortical and non-cortical labelled volumes as inputs. From an anatomical standpoint, the cortical labelled volume employed (cortical ribbon) is limited between an external outline corresponding to the outer layer of the cortex and an internal outline identified by the inner layer of the cerebral cortex adjacent to callosal WM fibres. The method identifies a continuous one-to-one correspondence between inner and outer cortical surfaces and the cortical thickness is estimated via a distance measure on the basis of this diffeomorphic correspondence. The inner surface is used as a reference to initialize a thin layer of about 1 voxel width. This layer, which replicates the shape

of the outer layer of the cortex, is then allowed to expand under the diffeomorphic deformation. The deformation is introduced through the cortical label until the layer reaches the outer cortical surface and the obtained deformation map can eventually be used to compute the cortical thickness. The final result of this process is a cortical voxelwise map with a nominal "thickness" value in each voxel, reflecting the deformation field that voxel has been subjected to (Das et al., 2009). Figure S2 shows an illustrative example of the obtained voxelwise cortical thickness map where the presence of parallel columns of voxels exhibiting constant thickness is apparent. The obtained maps are then typically cross-compared using standard voxelwise statistics. The original method (Das et al., 2009) was optimized to identify deep sulci of the human brain by forcing the algorithm to recover lost sulci, but can also be applied to map lissencephalic cortices like those of the rodent brain. The estimation process is carried out separately for right and left hemisphere to preserve the Neumann boundary (Lee et al., 2011).

The cortical thickness estimation includes four main steps. First, a right and the left cortical label need to be created, as well as the non-cortical label. In the present study this was achieved by combining all cortical labels mapped (enthorinal cortex, frontal, occipital and parieto-temporal lobe) of the Dorr MRI atlas of the mouse brain (Dorr et al., 2008) into one single hemispheric label. A non-cortical label was generated by merging all the remaining non-cortical regions. Second, cortical thickness is estimated using *KellyKapowsky*, with a prior anatomical constraint of cortical thickness of two millimetres and a gradient step size for optimisation of 0.02. Number of iterations, threshold and window size for convergence were left unchanged (e.g. default parameters). Third, maps of cortical thickness are combined into a joint volume and transformed to template space using available registration maps obtained previously. Fourth, the transformed cortical maps are smoothed using a Gaussian kernel with a sigma of two voxel width (FWHM=0.42). This process yields images that can be used for univariate or multivariate analysis at the voxel level.

Despite the use of non-callosal mice our automated anatomical labelling correctly labelled the cortical mantle of BTBR in virtually all cortical areas, with possible minor underestimations of cortical thickness in medial anterior cingulate regions. As a result, intergroup alterations in those regions may be interpreted cautiously when acallosal mice are used as reference strain. However most mouse lines commonly used in neuroscience and preclinical research exhibit normal callosal integrity and are therefore to be considered immune

to this potential artefact.

To further evaluate the accuracy of the cortical thickness estimation process, manual measurement was also performed by an experienced operator blinded to the results of the cortical thickness estimation (Figure 6). In a randomly chosen subject, three coronal slices were extracted and cortical thickness was measured for secondary motor cortex (M2), secondary somatosensory cortex (S2) and auditory cortex (Au) using the ruler tool available in the ITK Workbench.

2.4. Statistical analysis

All statistical analysis of the smoothed and modulated GM probability maps and cortical thickness maps were conducted using FSL. Firstly, maps were concatenated in a 4D dataset, using *fslmerge*. Subsequently, standard non-parametric Monte Carlo test with 5000 random permutations was performed using *randomise*. Threshold-free cluster enhancement was employed to include voxels' neighbourhood information without defining a-priori cluster threshold. P-values were corrected for multiple comparisons using a cluster-based threshold of 0.01 (Jenkinson et al., 2012; Worsley et al., 1992). Two-tailed voxelwise statistics were used for inter-group VBM and cortical thickness mapping. Brain volumes, resulting from the segmentation process, were tested for statistical differences between the two strains using a two-tailed Student's t-test, followed by Hochberg's correction for multiple comparisons.

3. Results

As an illustrative example of the approach, we tested our set of methods to map and quantify morphological variations in inbred socially impaired BTBR mice with respect to normosocial B6 (Squillace et al., 2014). A biological interpretation of the differences mapped has been recently reported by us (Dodero et al., 2013) and others (Ellegood et al., 2013), and will not be re-discussed here.

3.1. Study based template and volumetric analysis

A study based template created following the procedure herein explained is depicted in Figure 5. The template was created using the scans of nine normosocial B6 mice, which have been used as reference population for this illustrative study. The template reveals clear structural boundaries and high WM-GM contrast, depicting fine-grain anatomical features that can be used

to describe the population more effectively and reliably than a single representative subject (Tucci et al., 2014).

In pilot studies, we assessed the accuracy of registrations as a function of varying registration parameters (i.e. window radius and gradient step for symmetric normalization) as recently described (Badea et al., 2012). By varying registration parameters, the approach can be used to identify the best set of parameters matching the results of manual parcellation. We varied windows radius between 3 and 9 voxels, and gradient step for symmetric normalization between 0.10 and 2 voxels. The results of this analysis (Figure S3) show that the parameters choses (5 and 0.5 voxels, respectively) produce a good registration accuracy in all the brain regions tested. These parameters are in agreement with those previously selected by Badea and colleagues using *ex vivo* brain samples imaged at 9.4 Tesla.

Using these validated parameters, cross-strain volumetric analysis using anatomical labels from the two atlases highlighted the presence of a general reduction in cortical volume in BTBR mice with respect to B6 mice. Also major subcortical structures, including caudoputamen, hippocampus and hypothalamus reported a statistical significant reduction in volume (Figure 7). These results are in good agreement with recent comparative neuroanatomical mapping of these two strains performed by other labs (Ellegood et al., 2013), where a similar significant decrease in the volume of cortex and corpus callosum was shown.

3.2. VBM

Whole-brain VBM revealed widespread and bilateral reductions in GM volume across dorsofrontal, cingulate, retrosplenial, occipital and parietal cortex (Figure 8, $Z>3.1$, p-corrected$<.001$), in BTBR compared to B6 controls. These findings are in agreement with the results of anatomical labelling. GM volume reductions were also evident in subcortical areas, including the lateral and posterior thalamus (longitudinal fasciculus), the posterior hypothalamus and the ventral hippocampus. Interestingly, VBM highlighted also small bilateral foci of increased GM volume in the olfactory bulbs, in the medial pre-frontal and insular cortex, in the amygdala and in the dorsal hippocampus. The detection of small focal effects that could not be revealed when integrated over large anatomical volumes is one of the main advantages of the VBM approach over classic neuroanatomical volumetric mapping. These results are in good agreement with recent comparative neuroanatomical mapping of these two strains performed by

other labs using tensor based morphometry (Ellegood et al., 2013), which showed similar significant alterations (using Tensor Based Morphometry, see discussion below) in hippocampal and cortical areas.

3.3. Cortical Thickness Estimation

Further investigation of the presence of local alterations of GM in BTBR mice compared to B6 controls was performed in terms of cortical thickness estimation. Average spatially-normalized voxel-based thickness maps were calculated separately for each of the two strains and three-dimensionally rendered for visualization purposes (Figure 9). In good agreement with the results of automated anatomical labelling and VBM mapping, a widespread reduction in mean cortical thickness ($Z>2.3$, p-corrected<0.01) was observed in BTBR mice compared to B6 controls. Importantly, inter-group voxel-wise statistics revealed significantly increased cortical thickness in medial prefrontal and insular regions in the BTBR cohort ($Z>2.3$, p-corrected<0.01).

4. Discussion and conclusions

Here we described semi-automated procedures for automated anatomical labelling, VBM and cortical thickness estimation in the mouse brain. The approach has been recently applied to detect fine-grained morphoanatomical alterations in different mutant mouse lines, including alterations in β-catenin mouse mutants (Tucci et al., 2014), acallosal and socially-impaired mice (Dodero et al., 2013) and to identify sexually divergent effects on cortical anatomy in catechol-O-methyltransferase mutant lines (Sannino et al., 2014). In the latter study, we showed remarkably consistent intergroup differences in regional GM volume as assessed with our VBM pipeline, or manual morphometric measurements of cortical thickness in post-mortem brain slices (Sannino et al., 2014), thus underscoring the accuracy and sensitivity of our workflow.

The image processing described here adopts the methodologies and toolkits originally developed for human brain imaging and can be straightforwardly extended to other areas of research and mouse models of disease. For example, we also used VBM to describe symmetric networks of anatomical covariance in the cortex of inbred mice complementary to those previously identified in humans, providing a new tool to study gray matter disrupted connectivity in brain disorders with transgenic mice (Pagani et al., 2016). Although prominent examples of the use of morphoanatomical methods in the mouse have been recently described by other labs

(Badea et al., 2012; Borg and Chereul, 2008; Budin et al., 2013; Delatour et al., 2006; Johnson et al., 2007; Lee et al., 2010; Lerch et al., 2011a; Nieman et al., 2005; Oguz and Sonka, 2014; Sawiak et al., 2009; Sawiak et al., 2013), the vast majority of these contribution lack a detailed description of the complex workflow required to process and analyse different morphoanatomical readouts, thus complicating the replication of these methods by other groups. The methodological workflow presented in this work was designed to facilitate the implementation of fine-grained morphoanatomical mapping tools by non-expert users, and promote forward and back translation of MRI preclinical and clinical research evidence. We also point out that a preliminary account on the implementation of these procedures in parallel computing cloud environment has been recently reported (Minervini et al., 2014), a strategy that can streamline and accelerate image processing time by exploiting large high-performance-computing infrastructures.

A dominant feature of our unified approach is the coupling of standard intensity based affine registration with a symmetric diffeomorphic normalization algorithm to obtain optimal MR image registration (Avants et al., 2008). This approach, which has been successfully employed both in human (Kim et al., 2008; Klein et al., 2009; Klein et al., 2010) and small animal imaging studies (Avants et al., 2010b; Lerch et al., 2011b), is based on the ANTs open source software library and is adopted to create a study based template, carry out skull stripping and perform anatomical labelling via label propagation. Our cortical thickness estimation approach is also registration-based, and employs *DiReCT*, an advanced diffeomorphic registration algorithm implemented in ANTs toolkit that has been recently validated on human imaging data (Das et al., 2009) and used for research studies with clinical population (Avants et al., 2010a). To the best of our knowledge, this is the first example of the application of this approach to map cortical thickness in small rodent species.

The cortical thickness mapping and anatomical labelling approaches employed rely on the availability of three dimensional labelled MRI atlases with delineated cortical and subcortical morphology. While a universally accepted MRI atlas of the mouse brain is still not available, a number of mouse brain MRI atlases have been published based on high resolution acquisitions of a single subject (Badea et al., 2012; Maheswaran et al., 2009a; Xie et al., 2010; Zhang et al., 2010) or constructed from several animals, with data gathered either *in vivo* (Aggarwal et al., 2009; Ma et al., 2008; Maheswaran et al., 2009b) or from *ex vivo* fixed specimens (Aggarwal et

al., 2009; Badea et al., 2007; Dorr et al., 2008; Johnson et al., 2010; Kovacevic et al., 2005; Ullmann et al., 2013). In this study, a combination of two atlases was employed to obtain a fine-grained parcellation of both cortical (Ullmann et al., 2013) and subcortical (Dorr et al., 2008; Ullmann et al., 2013) regions. However, our method is not atlas-dependent and can be flexibly adapted to a number of published or custom mouse brain MRI anatomical partitions.

An important benefit of our approach is the possibility to measure different and complementary morphoanatomical brain metrics - including volumetric analysis, VBM and cortical thickness - in a single reference space. This aspect is of crucial importance, as it broadens the scope of application of MRI-based brain morphometry and it augments its translational potential by permitting a multi parametric comparison with analogous clinical readouts. In the illustrative example reported here, an overall agreement between the three readouts was found. Apparent discrepancies between readouts (e.g., the lack of inter-strain differences in insular volume, due to the presence of VBM foci of increased and decreased regional volume in anterior and posterior portions of this region) are the result of different sampling scales (label vs. voxel level) of the readouts employed. We also note that the combination of complementary approaches can help disambiguate morphological alterations of pathological origin, as the relationship between thickness and local GM volume has not been thoroughly clarified, and may probably change across pathologies and populations (Hutton et al., 2008). Within this scenario, the use of complementary metrics coupled to histological staining can help to pinpoint the pathological bases of brain morphometric changes of neuropathological origin.

In addition, our preprocessing workflow can be straightforwardly extended to perform tensor based morphometry (TBM). As in VBM, TBM entails the local computation of the Jacobian determinants of the deformation field used to map subjects' images to the study based template. The Jacobian determinant (i.e. the local scaling factor) encodes for local anatomical expansions and contractions of subjects' areas relative to the study based template, and therefore Jacobian maps can be used to localise inter-group differences in the local shape of brain structures at the voxel level. TBM analysis can be simply performed by omitting the tissue segmentation step in the VBM procedure herein described. As TBM does not entail tissue classification, it can be used for the simultaneous investigation of WM and GM alterations, and may robustly detect alterations in areas of mixed WM-GM structures, such as the thalamus and

brain stem, which are especially sensitive to the accuracy of intensity based tissue classification algorithms.

A few methodological limitations in our approach deserved to be mentioned. The procedure described here has been developed and optimized or fixed *ex vivo* brain samples imaged at 7 Tesla using T2-weighted images. While the application of our workflow to different field strengths and image contrast is conceivable, adjustments in single preprocessing parameters may be required to adapt our procedure to different contrast mechanisms or images acquired at different field strengths. One limitation of our cortical thickness mapping is its poor performance in resolving thickness at the level of inter-hemispheric fissure in medial regions of the mouse cortex such as cingulate or retrosplenial areas (Figure S2). As a result, inter-group differences in cortical thickness in these regions should be interpreted with caution. Researchers interested in mapping gray matter alterations in these regions with high confidence, should consider cross validating thickness mapping with voxelwise methods described in our workflow that are immune to this limitation, such as VBM and TBM. Similarly, the segmentation of the anterior cingulate in acallosal mice such as BTBR should be considered tentative, as the lack of clear white matter gray matter boundary prevents an empirical assessment of its accuracy. Once again, voxelwise-based morphoanatomical mapping together with histological measurements can help validate cortical thickness measurements in these areas when acallosal mice are employed. Caution should also be exercised in interpreting inter-group differences in mouse models characterized by profound demyelination and neurodegeneration, two conditions that can reduce GM/WM contrast and affect segmentation accuracy for VBM. Notwithstanding these limitations, the possibility of using a unified workflow to map multiple complementary morphoanatomical parameters should be emphasized as a major point of strength of our approach, owing to the possibility of cross-comparing different readouts to dissect specific neuroanatomical features with increased confidence.

In conclusion, we described a registration-based approach for anatomical mapping, VBM and cortical thickness estimation in the mouse brain. The application of these procedures enabled the identification of subtle volumetric differences across subjects without prior knowledge of structures of interest. Our unified approach based on diffeomorphic registration permits to integrate complementary MR morphoanatomical techniques, and is based on popular open source software (ANTs), which has been extensively employed in priori MRI morphometric

studies. The detailed operational workflow described in the present work is expected to help the implementation of rodent morphoanatomical methods by non-expert users, thus ultimately promoting the use of these tools across the preclinical neuroimaging community.

Captions

Figure 1. Preprocessing workflow.

Each MRI subject image undergoes a first correction for intensity non-uniformity bias using the *N3BiasFieldCorrection*. To create individual subject masks, a masked representative reference subject is registered to each subject, and the transformation of this registration is then applied to the reference subject mask. The application of this mask permits to remove most extra brain tissue. Non-uniformity bias is subsequently estimated for individual masked brains. The preprocessing procedure outputs a skull-stripped bias-corrected image and a companion binary brain mask for each subject.

Figure 2. Preprocessing results.

In this illustrative example, the original subject image (a) is bias corrected before (b) and after (e) skull stripping (d). Note the improved bias field correction after skull stripping (f) with respect to the bias correction prior skull stripping (c), especially in the ventral part of the brain and in the ventricles. Voxels intensity is represented in shades of red to magnify image contrast.

Figure 3. Automated anatomical labelling and cortical thickness estimation.

Upper box: Anatomical labels of the MRI atlas are registered into each subject space via the study based template through a combination of linear and diffeomorphic mapping, using *antsRegistration* and *WarpImageMultiTransform*. A propagation of the labels from the MRI atlas to each subject space is then performed via the study based template, followed by the estimation of the volume for each label. Lower box: Anatomical labels of the cortical mantle in the subject space are merged together to build a unified cortical label. This cortical label and subject brain mask of the subjects are used to create the inputs needed to estimate the cortical thickness using *DiReCT*. The obtained cortical thickness maps are eventually warped again into the study based space and smoothed for subsequent statistical comparison.

Figure 4. VBM.

Each preprocessed subject image is mapped on the study based template space through a combination of linear and diffeomorphic mapping, using *antsRegistration* and *WarpImageMultiTransform*. Registered volumes are segmented using the study based template priors. Grey matter probability maps for each subject are then modulated using Jacobian maps obtained from the registration process and smoothed for subsequent statistical comparison.

Figure 5. Study based template and tissue segmentation.

Orthogonal slice view of a study based template of the B6 mice population obtained using the iterative diffeomorphic registration process of the *buildtemplateparallel* script and its corresponding tissue segmentation (a). The template is segmented using *Atropos* in 6 different tissue classes which are used as a-priori information for individual estimation of gray matter in VBM. The different tissue classes of the template are combined to obtain gray matter (b) and non gray matter components (c, white matter, plus ventricular regions and CSF).

Figure 6. Correlation plot between *DiReCT* outputs and manual measurements of cortical thickness.
Secondary motor (M2), secondary somatosensory (S2) and auditory cortex (Au) were chosen as representative cortical areas to validate our cortical thickness methodology. Representative measures from DiReCT and manual estimates are reported for selected cortical regions (middle panel). A correlation plot of manual and automatic measurements highlighted an excellent correspondence between the twee readouts in terms of Pearson's correlation ($r=0.99$; $p<0.001$).

Figure 7. Anatomical labelling.
The labels of the reference atlas employed are warped into subjects' space via the study based template using the combination of affine and diffeomorphic mapping obtained after the registration process. The registered labels permit to calculate volumes of brain areas of interest and perform t-tests between the mouse samples. (Cpu: caudoputamen; Th: thalamus; OB: olfactory bulbs; HP: hippocampus; Hyp: hypothalamus, CC: corpus callosum; OF: orbitofrontal cortex; RS: retrosplenial cortex; M1: primary motor cortex; V1: primary visual cortex; Rh: rhinal cortex). **p<.01; ***p<.001.)

Figure 8. VBM.
Differences in local gray matter volumes are assessed combining gray matter probability maps and local Jacobian determinants. Statistical comparison (p<.01, threshold-free cluster enhancement followed by cluster-based thresholding) showed widespread and bilateral reductions in grey matter volumes across dorsofrontal, cingulate, retrosplenial, occipital and parietal cortex as well as in subcortical structures in BTBR compared to B6 controls. VBM highlighted also small bilateral foci of increased gray matter volume in the olfactory bulbs, in the medial pre-frontal and insular cortex, in the amygdala and in the dorsal hippocampus. (Cb: cerebellum; Cpu: caudoputamen; DHyp: dorsal hypothalamus; dPFC: dorsal prefrontal cortex; LTh: lateral thalamus; mPFC: medial prefrontal cortex; OB: olfactory bulbs; Rh: rhinal cortex; RS: retrosplenial cortex).

Figure 9. Cortical thickness estimation.
Three-dimensional rendering views of average cortical thickness in BTBR and B6 mice (a). Statistical comparison showed significant cortical thickness thinning (p<0.01, threshold-free cluster enhancement followed by cluster-based thresholding) in parietal, temporal and peri-hippocampal cortex of BTBR mice. Increased thickness was observed in medial prefrontal and anterior insular regions of this strain (b).

Figure S1. Segmentation of the study based template using six tissue classes provides accurate GM/WM separation.
A: Standard three-class segmentation of our ex vivo brains using Atropos did not produce an accurate GM/WM separation, with a great overestimation of white matter fraction. Anatomical template (left), plus the segmentation classes obtained with a three-cluster segmentation approach (WM, mixed WM/GM and GM matter maps, from left to right, respectively). B: The combined use of six independent segmentation classes leads to a more accurate

separation of GM and WM. The final GM map is the combined result of three GM classes (middle row). Additional non-GM tissue can be obtained by merging the remaining three classes.

Figure S2. Cortical thickness estimation.

In lissencephalic brains, DiReCT measurement results in a string of voxels exhibiting constant thickness. This appears in the form of parallel cortical "columns" in coronal brain slices clearly visible in the magnified view, where colors represent the norm of the deformation field that is the estimated thickness.

Figure S3. Optimization of registration parameters for anatomical labelling.

Accuracy of registration (Dice coefficient) for varying registration parameters (window radius for cross correlation and gradient steps). Top: as in Badea et al., (2012), we varied windows radius between 3 and 9 voxels. The chosen value (5 voxels) produces a good performance in all the brain regions tested. Bottom: the gradient step parameter for the symmetric normalization was varied between 0.10 and 2 voxels. The chosen parameter (0.5 voxels) produces a good performance in all the tested regions.

References

Aggarwal M, Zhang J, Miller MI, Sidman RL, Mori S. Magnetic resonance imaging and micro-computed tomography combined atlas of developing and adult mouse brains for stereotaxic surgery. Neuroscience, 2009; 162: 1339-50.

Ashburner J, Friston KJ. Voxel-based morphometry--the methods. Neuroimage, 2000; 11: 805-21.

Avants BB, Cook PA, Ungar L, Gee JC, Grossman M. Dementia induces correlated reductions in white matter integrity and cortical thickness: a multivariate neuroimaging study with sparse canonical correlation analysis. Neuroimage, 2010a; 50: 1004-16.

Avants BB, Epstein CL, Grossman M, Gee JC. Symmetric diffeomorphic image registration with cross-correlation: Evaluating automated labeling of elderly and neurodegenerative brain. Medical Image Analysis, 2008; 12: 26-41.

Avants BB, Tustison N, Song G. Advanced normalization tools (ANTS). Insight J, 2009.

Avants BB, Tustison NJ, Stauffer M, Song G, Wu B, Gee JC. The Insight ToolKit image registration framework. Frontiers in neuroinformatics, 2014; 8.

Avants BB, Tustison NJ, Wu J, Cook PA, Gee JC. An open source multivariate framework for n-tissue segmentation with evaluation on public data. Neuroinformatics, 2011; 9: 381-400.

Avants BB, Yushkevich P, Pluta J, Minkoff D, Korczykowski M, Detre J, Gee JC. The optimal template effect in hippocampus studies of diseased populations. Neuroimage, 2010b; 49: 2457-66.

Badea A, Ali-Sharief AA, Johnson GA. Morphometric analysis of the C57BL/6J mouse brain. Neuroimage, 2007; 37: 683-93.

Badea A, Gewalt S, Avants BB, Cook JJ, Johnson GA. Quantitative mouse brain phenotyping based on single and multispectral MR protocols. Neuroimage, 2012; 63: 1633-45.

Borg J, Chereul E. Differential MRI patterns of brain atrophy in double or single transgenic mice for APP and/or SOD. J Neurosci Res, 2008; 86: 3275-84.

Budin F, Hoogstoel M, Reynolds P, Grauer M, O'Leary-Moore SK, Oguz I. Fully automated rodent brain MR image processing pipeline on a Midas server: from acquired images to region-based statistics. Front Neuroinform, 2013; 7: 15.

Cahill LS, Laliberté CL, Ellegood J, Spring S, Gleave JA, van Eede MC, Lerch JP, Henkelman RM. Preparation of fixed mouse brains for MRI. Neuroimage, 2012; 60: 933-9.

Chou C-H, Su M-C, Lai E. A new cluster validity measure and its application to image compression. Pattern Analysis and Applications, 2004; 7: 205-20.

Cutuli D, Pagani M, Caporali P, Galbusera A, Laricchiuta D, Foti F, Neri C, Spalletta G, Caltagirone C, Petrosini L. Effects of Omega-3 Fatty Acid Supplementation on Cognitive Functions and Neural Substrates: A Voxel-Based Morphometry Study in Aged Mice. Frontiers in aging neuroscience, 2016; 8.

Das SR, Avants BB, Grossman M, Gee JC. Registration based cortical thickness measurement. Neuroimage, 2009; 45: 867-79.

Delatour B, Guegan M, Volk A, Dhenain M. In vivo MRI and histological evaluation of brain atrophy in APP/PS1 transgenic mice. Neurobiol Aging, 2006; 27: 835-47.

Dice LR. Measures of the amount of ecologic association between species. Ecology, 1945; 26: 297-302.

Dodero L, Damiano M, Galbusera A, Bifone A, Tsaftsaris SA, Scattoni ML, Gozzi A. Neuroimaging evidence of major morpho-anatomical and functional abnormalities in the BTBR T+TF/J mouse model of autism. PLoS One, 2013; 8.

Dorr AE, Lerch JP, Spring S, Kabani N, Henkelman RM. High resolution three-dimensional brain atlas using an average magnetic resonance image of 40 adult C57Bl/6J mice. Neuroimage, 2008; 42: 60-9.

670 Ellegood J, Babineau BA, Henkelman RM, Lerch JP, Crawley JN. Neuroanatomical analysis of
671 the BTBR mouse model of autism using magnetic resonance imaging and diffusion tensor
672 imaging. Neuroimage, 2013; 70: 288-300.
673 Friston KJ, Holmes AP, Worsley KJ, Poline JP, Frith CD, Frackowiak RS. Statistical parametric
674 maps in functional imaging: a general linear approach. Human brain mapping, 1994; 2: 189-
675 210.
676 Hutton C, De Vita E, Ashburner J, Deichmann R, Turner R. Voxel-based cortical thickness
677 measurements in MRI. Neuroimage, 2008; 40: 1701-10.
678 Jenkinson M, Beckmann CF, Behrens TE, Woolrich MW, Smith SM. Fsl. Neuroimage, 2012; 62:
679 782-90.
680 Jia H, Yap PT, Wu G, Wang Q, Shen D. Intermediate templates guided groupwise registration
681 of diffusion tensor images. Neuroimage, 2011; 54: 928-39.
682 Johnson GA, Ali-Sharief A, Badea A, Brandenburg J, Cofer G, Fubara B, Gewalt S, Hedlund
683 LW, Upchurch L. High-throughput morphologic phenotyping of the mouse brain with magnetic
684 resonance histology. Neuroimage, 2007; 37: 82-9.
685 Johnson GA, Badea A, Brandenburg J, Cofer G, Fubara B, Liu S, Nissanov J. Waxholm space:
686 an image-based reference for coordinating mouse brain research. Neuroimage, 2010; 53:
687 365-72.
688 Kim J, Avants B, Patel S, Whyte J, Coslett BH, Pluta J, Detre JA, Gee JC. Structural
689 consequences of diffuse traumatic brain injury: a large deformation tensor-based
690 morphometry study. Neuroimage, 2008; 39: 1014-26.
691 Klein A, Andersson J, Ardekani BA, Ashburner J, Avants B, Chiang M-C, Christensen GE,
692 Collins DL, Gee J, Hellier P. Evaluation of 14 nonlinear deformation algorithms applied to
693 human brain MRI registration. Neuroimage, 2009; 46: 786-802.
694 Klein A, Ghosh SS, Avants B, Yeo BT, Fischl B, Ardekani B, Gee JC, Mann JJ, Parsey RV.
695 Evaluation of volume-based and surface-based brain image registration methods.
696 Neuroimage, 2010; 51: 214-20.
697 Kovacevic N, Henderson JT, Chan E, Lifshitz N, Bishop J, Evans AC, Henkelman RM, Chen XJ.
698 A three-dimensional MRI atlas of the mouse brain with estimates of the average and
699 variability. Cereb Cortex, 2005; 15: 639-45.
700 Lassi G, Priano L, Maggi S, Garcia-Garcia C, Balzani E, El-Assawy N, Pagani M, Tinarelli F,
701 Giardino D, Mauro A. Deletion of the Snord116/SNORD116 Alters Sleep in Mice and Patients
702 with Prader-Willi Syndrome. Sleep, 2015.
703 Lee D, Ruffins S, Ng Q, Sane N, Anderson S, Toga A. MBAT: a scalable informatics system for
704 unifying digital atlasing workflows. BMC Bioinformatics, 2010; 11: 1471-2105.
705 Lee J, Ehlers C, Crews F, Niethammer M, Budin F, Paniagua B, Sulik K, Johns J, Styner M,
706 Oguz I. Automatic cortical thickness analysis on rodent brain. Proc Soc Photo Opt Instrum
707 Eng, 2011; 15: 7962481-79624811.
708 Lerch JP, Carroll JB, Dorr A, Spring S, Evans AC, Hayden MR, Sled JG, Henkelman RM.
709 Cortical thickness measured from MRI in the YAC128 mouse model of Huntington's disease.
710 Neuroimage, 2008; 41: 243-51.
711 Lerch JP, Gazdzinski L, Germann J, Sled JG, Henkelman RM, Nieman BJ. Wanted dead or
712 alive? The tradeoff between in-vivo versus ex-vivo MR brain imaging in the mouse. Front
713 Neuroinform, 2012; 6: 6.
714 Lerch JP, Sled JG, Henkelman RM. MRI phenotyping of genetically altered mice. Magnetic
715 Resonance Neuroimaging. Springer, 2011a: 349-61.
716 Lerch JP, Yiu AP, Martinez-Canabal A, Pekar T, Bohbot VD, Frankland PW, Henkelman RM,
717 Josselyn SA, Sled JG. Maze training in mice induces MRI-detectable brain shape changes
718 specific to the type of learning. Neuroimage, 2011b; 54: 2086-95.
719 Li Q, Cheung C, Wei R, Hui ES, Feldon J, Meyer U, Chung S, Chua SE, Sham PC, Wu EX.
720 Prenatal immune challenge is an environmental risk factor for brain and behavior change

relevant to schizophrenia: evidence from MRI in a mouse model. PLoS One, 2009; 4: e6354.
Ma Y, Smith D, Hof PR, Foerster B, Hamilton S, Blackband SJ, Yu M, Benveniste H. In Vivo 3D Digital Atlas Database of the Adult C57BL/6J Mouse Brain by Magnetic Resonance Microscopy. Front Neuroanat, 2008; 2.
Maheswaran S, Barjat H, Bate ST, Aljabar P, Hill DL, Tilling L, Upton N, James MF, Hajnal JV, Rueckert D. Analysis of serial magnetic resonance images of mouse brains using image registration. Neuroimage, 2009a; 44: 692-700.
Maheswaran S, Barjat H, Rueckert D, Bate ST, Howlett DR, Tilling L, Smart SC, Pohlmann A, Richardson JC, Hartkens T, Hill DL, Upton N, Hajnal JV, James MF. Longitudinal regional brain volume changes quantified in normal aging and Alzheimer's APP x PS1 mice using MRI. Brain Res, 2009b; 13: 19-32.
Minervini M, Rusu C, Damiano M, Tucci V, Bifone A, Gozzi A, Tsaftaris SA. Large-scale analysis of neuroimaging data on commercial clouds with content-aware resource allocation strategies. International Journal of High Performance Computing Applications, 2014: 1094342013519483.
Mueller S, Keeser D, Reiser MF, Teipel S, Meindl T. Functional and structural MR imaging in neuropsychiatric disorders, part 2: application in schizophrenia and autism. AJNR Am J Neuroradiol, 2012; 33: 2033-7.
Nestler EJ, Hyman SE. Animal models of neuropsychiatric disorders. Nat Neurosci, 2010; 13: 1161-9.
Nieman BJ, Bock NA, Bishop J, Chen XJ, Sled JG, Rossant J, Henkelman RM. Magnetic resonance imaging for detection and analysis of mouse phenotypes. NMR Biomed, 2005; 18: 447-68.
Oguz I, Sonka M. LOGISMOS-B: layered optimal graph image segmentation of multiple objects and surfaces for the brain. IEEE Trans Med Imaging, 2014; 33: 1220-35.
Pagani M, Bifone A, Gozzi A. Structural covariance networks in the mouse brain. Neuroimage, 2016.
Sannino S, Gozzi A, Cerasa A, Piras F, Scheggia D, Manago F, Damiano M, Galbusera A, Erickson LC, De Pietri Tonelli D, Bifone A, Tsaftaris SA, Caltagirone C, Weinberger DR, Spalletta G, Papaleo F. COMT Genetic Reduction Produces Sexually Divergent Effects on Cortical Anatomy and Working Memory in Mice and Humans. Cereb Cortex, 2014; 21: 21.
Sawiak S, Wood N, Williams G, Morton A, Carpenter T. SPMMouse: A new toolbox for SPM in the animal brain. ISMRM 17th Scientific Meeting & Exhibition, April, 2009: 18-24.
Sawiak SJ, Wood NI, Williams GB, Morton AJ, Carpenter TA. Voxel-based morphometry with templates and validation in a mouse model of Huntington's disease. Magnetic Resonance Imaging, 2013; 31: 1522-31.
Sforazzini F, Bertero A, Dodero L, David G, Galbusera A, Scattoni ML, Pasqualetti M, Gozzi A. Altered functional connectivity networks in acallosal and socially impaired BTBR mice. Brain Structure and Function, 2014a: 1-14.
Sforazzini F, Schwarz AJ, Galbusera A, Bifone A, Gozzi A. Distributed BOLD and CBV-weighted resting-state networks in the mouse brain. Neuroimage, 2014b; 87: 403-15.
Squillace M, Dodero L, Federici M, Migliarini S, Errico F, Napolitano F, Krashia P, Di Maio A, Galbusera A, Bifone A, Scattoni ML, Pasqualetti M, Mercuri NB, Usiello A, Gozzi A. Dysfunctional dopaminergic neurotransmission in asocial BTBR mice. Transl Psychiatry, 2014; 4: e427.
Tucci V, Kleefstra T, Hardy A, Heise I, Maggi S, Willemsen MH, Hilton H, Esapa C, Simon M, Buenavista MT, McGuffin LJ, Vizor L, Dodero L, Tsaftaris S, Romero R, Nillesen WN, Vissers LE, Kempers MJ, Vulto-van Silfhout AT, Iqbal Z, Orlando M, Maccione A, Lassi G, Farisello P, Contestabile A, Tinarelli F, Nieus T, Raimondi A, Greco B, Cantatore D, Gasparini L, Berdondini L, Bifone A, Gozzi A, Wells S, Nolan PM. Dominant beta-catenin mutations cause intellectual disability with recognizable syndromic features. J Clin Invest, 2014; 124: 1468-82.

772 Ullmann JF, Watson C, Janke AL, Kurniawan ND, Reutens DC. A segmentation protocol and
773 MRI atlas of the C57BL/6J mouse neocortex. Neuroimage, 2013; 78: 196-203.
774 Worsley KJ, Evans AC, Marrett S, Neelin P. A three-dimensional statistical analysis for CBF
775 activation studies in human brain. Journal of Cerebral Blood Flow and Metabolism, 1992; 12:
776 900-.
777 Wu K-L, Yang M-S. A cluster validity index for fuzzy clustering. Pattern Recognition Letters,
778 2005; 26: 1275-91.
779 Xie Z, Yang D, Stephenson D, Morton D, Hicks C, Brown T, Bocan T. Characterizing the
780 regional structural difference of the brain between tau transgenic (rTg4510) and wild-type
781 mice using MRI. Med Image Comput Comput Assist Interv, 2010; 13: 308-15.
782 Yushkevich PA, Piven J, Hazlett HC, Smith RG, Ho S, Gee JC, Gerig G. User-guided 3D active
783 contour segmentation of anatomical structures: significantly improved efficiency and reliability.
784 Neuroimage, 2006; 31: 1116-28.
785 Zhang J, Peng Q, Li Q, Jahanshad N, Hou Z, Jiang M, Masuda N, Langbehn DR, Miller MI, Mori
786 S, Ross CA, Duan W. Longitudinal characterization of brain atrophy of a Huntington's disease
787 mouse model by automated morphological analyses of magnetic resonance images.
788 Neuroimage, 2010; 49: 2340-51.
789
790

Figure 1

Click here to download high resolution image

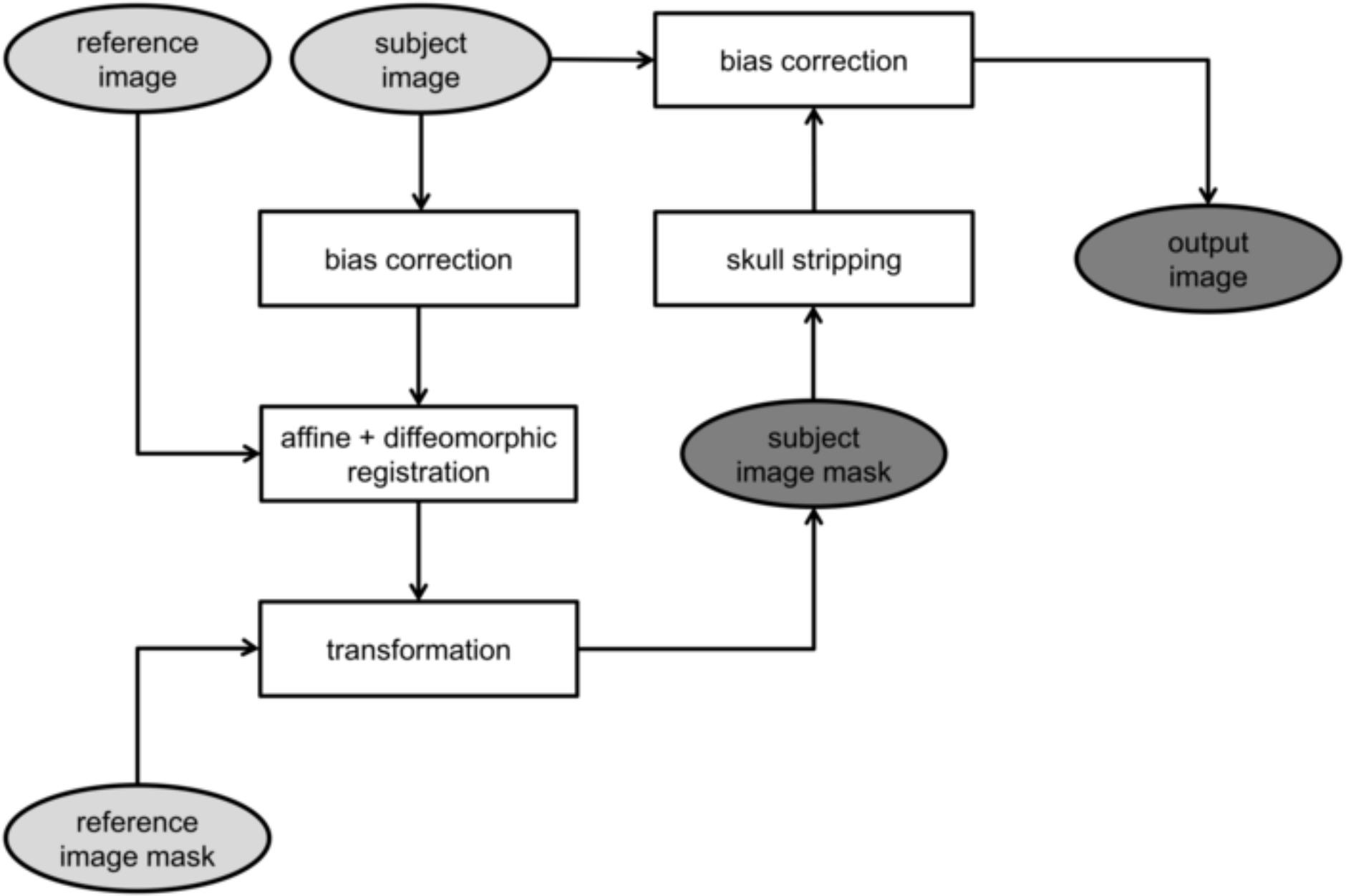

Figure 2
Click here to download high resolution image

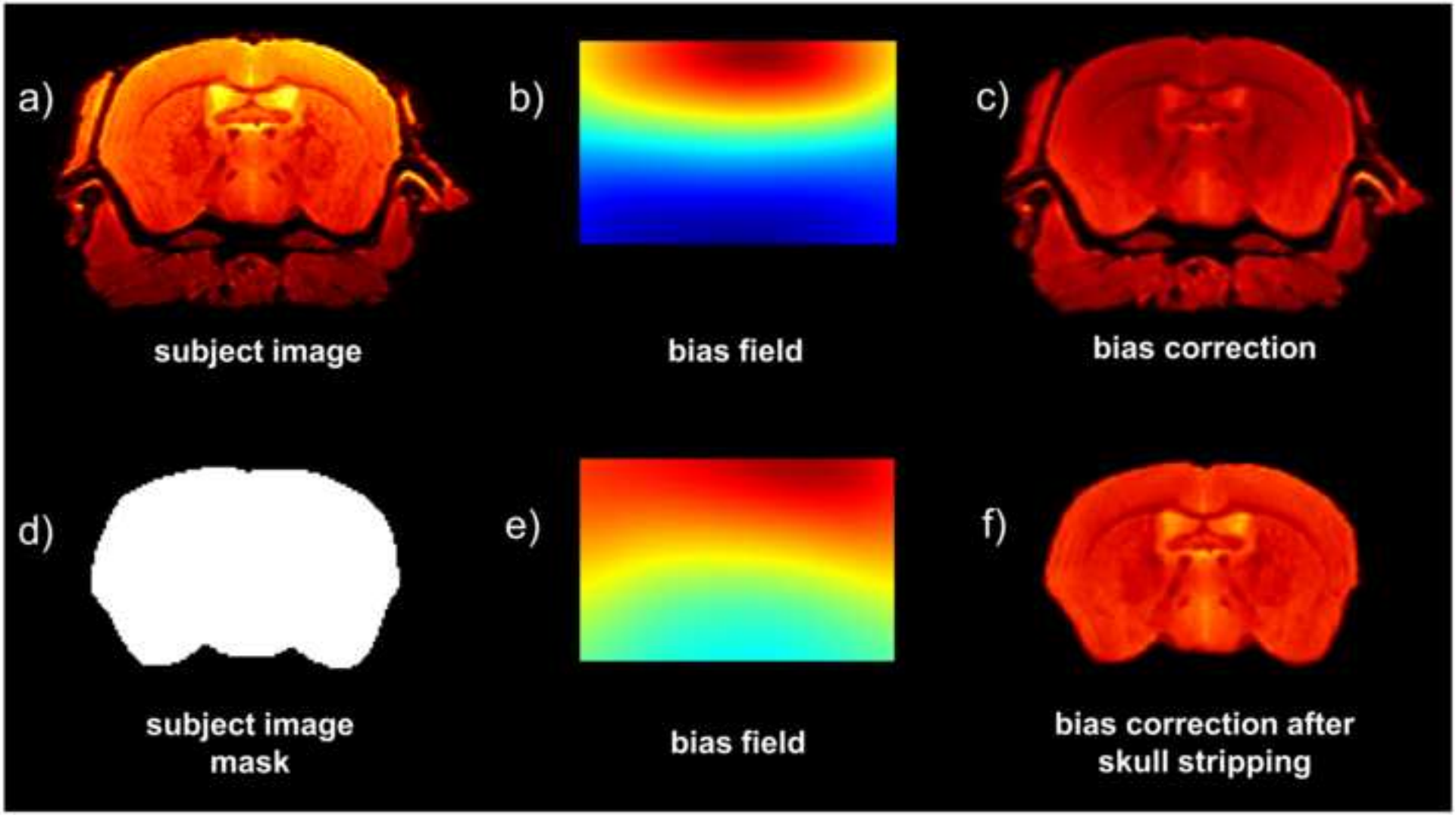

Figure 3

Click here to download high resolution image

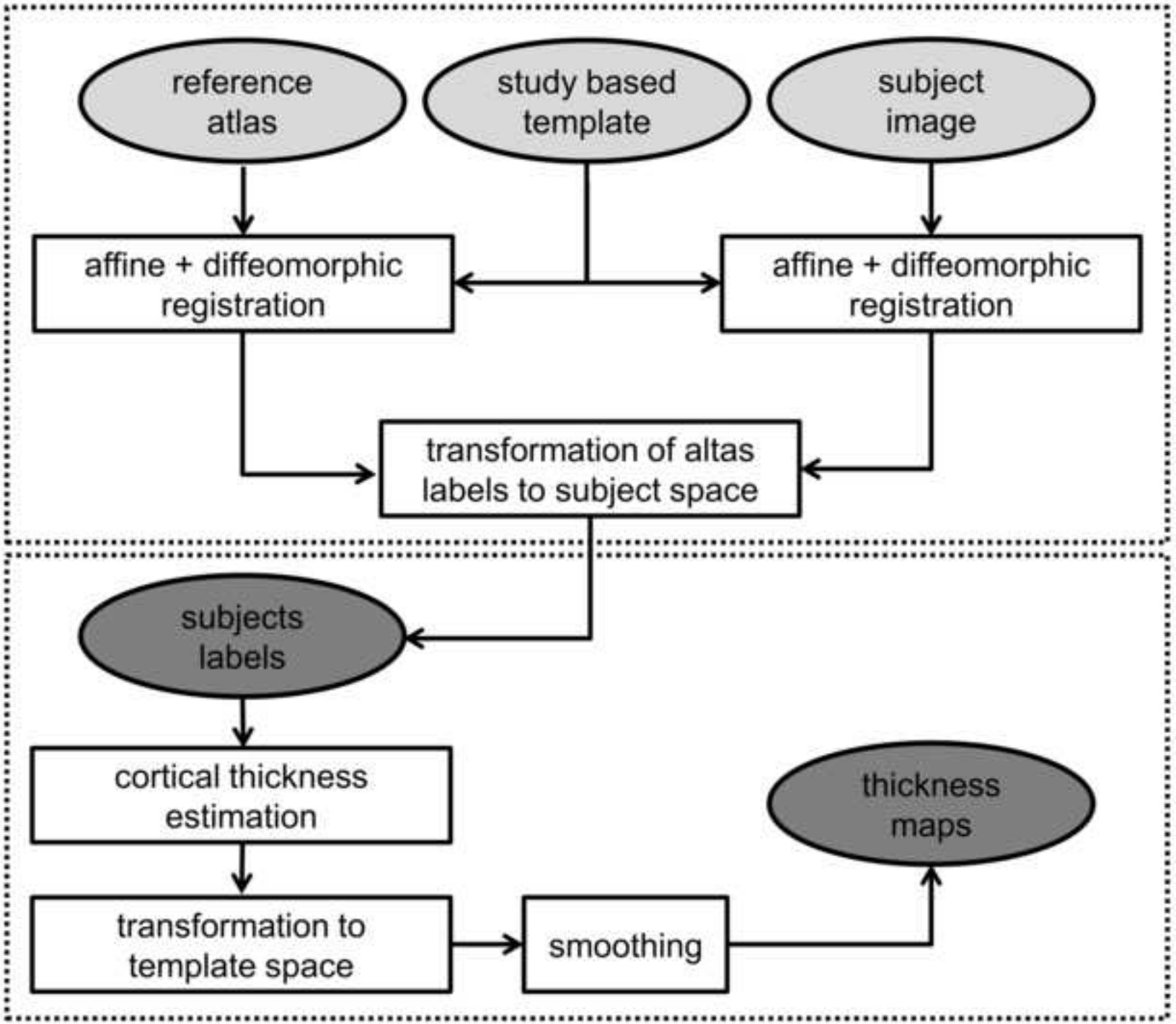

Figure 4

Click here to download high resolution image

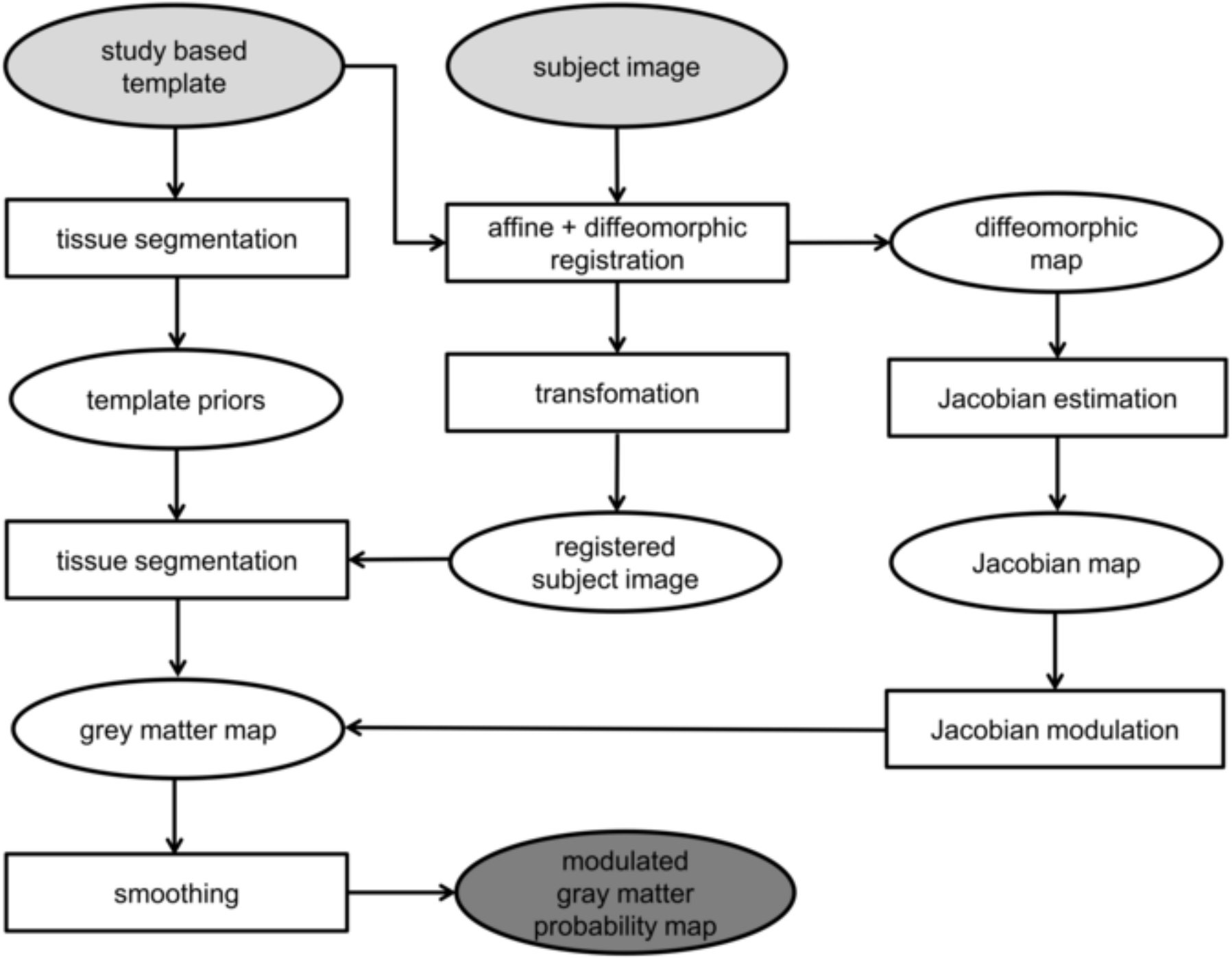

Figure 5

Click here to download high resolution image

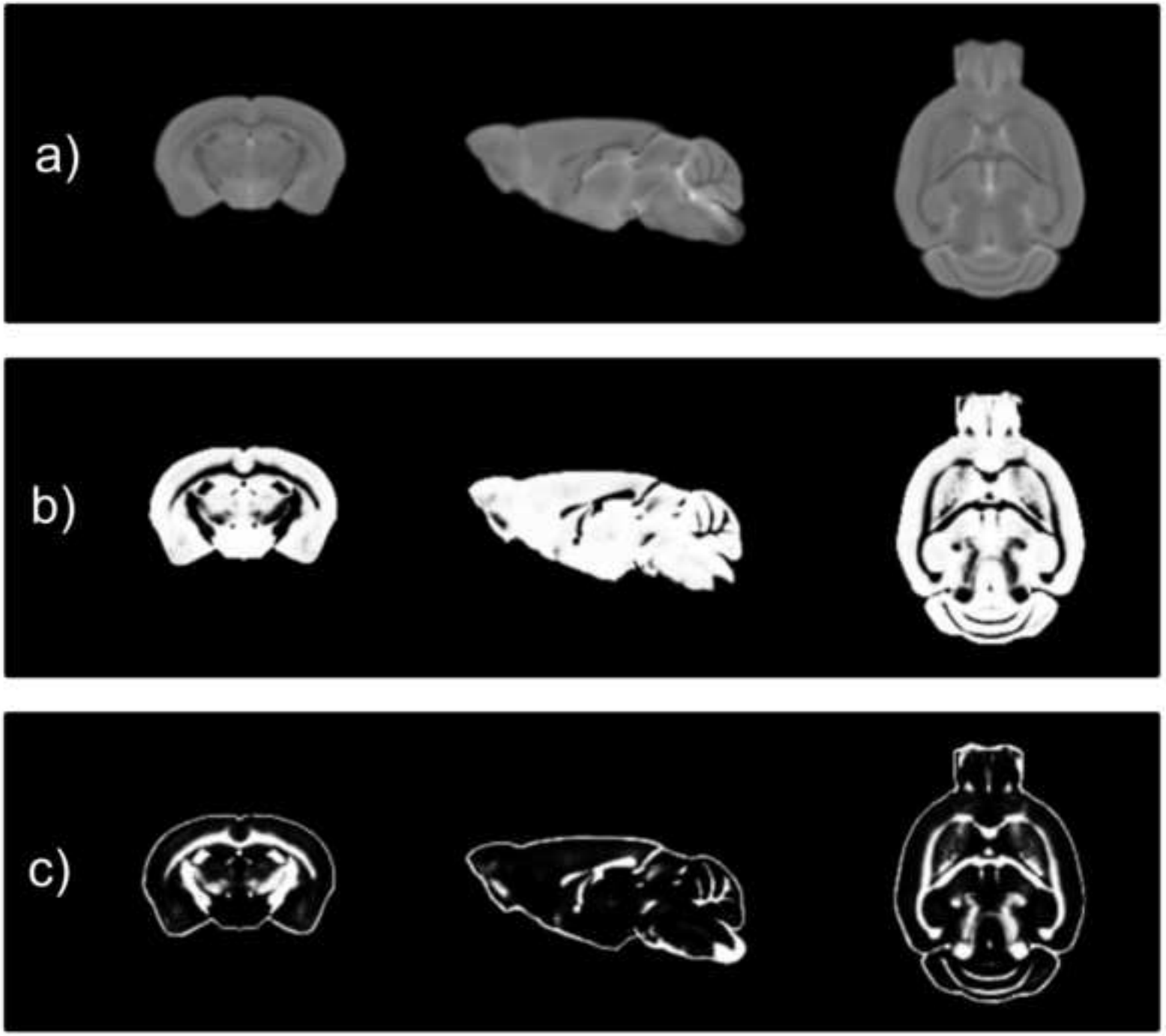

Figure 6

Click here to download high resolution image

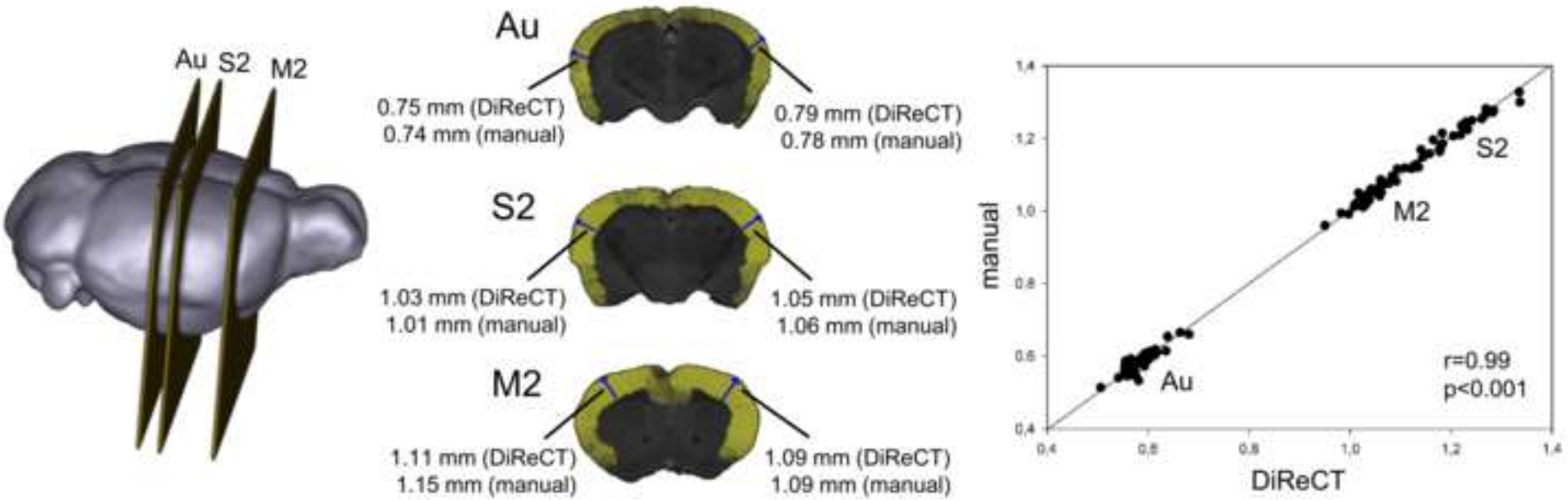

Figure 7

Click here to download high resolution image

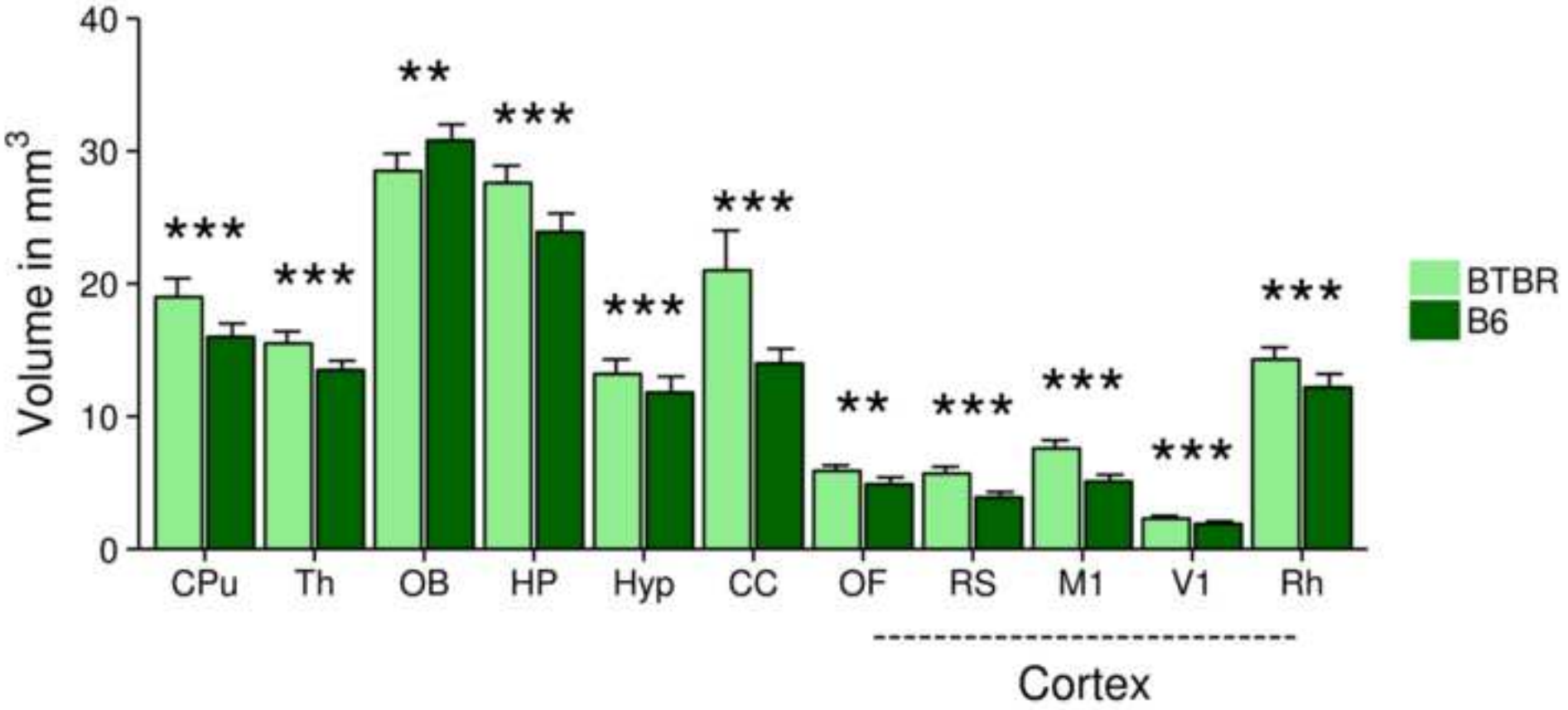

Figure 8

Click here to download high resolution image

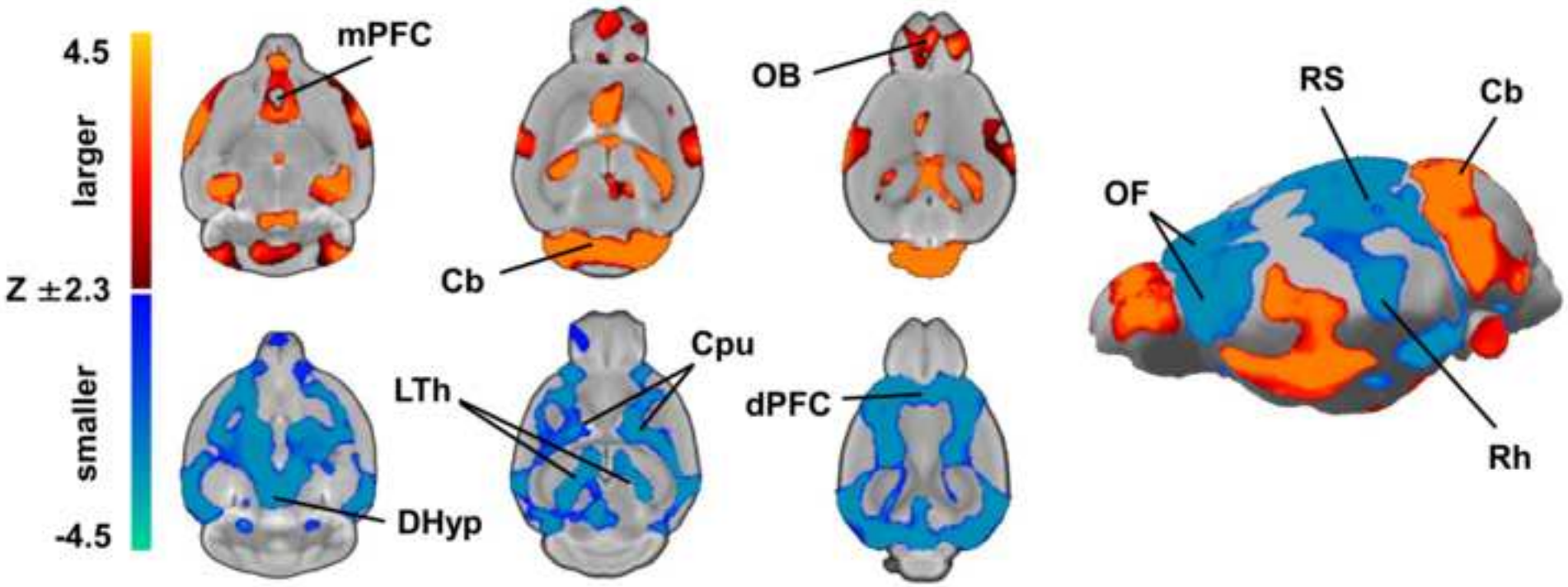

Figure 9
Click here to download high resolution image

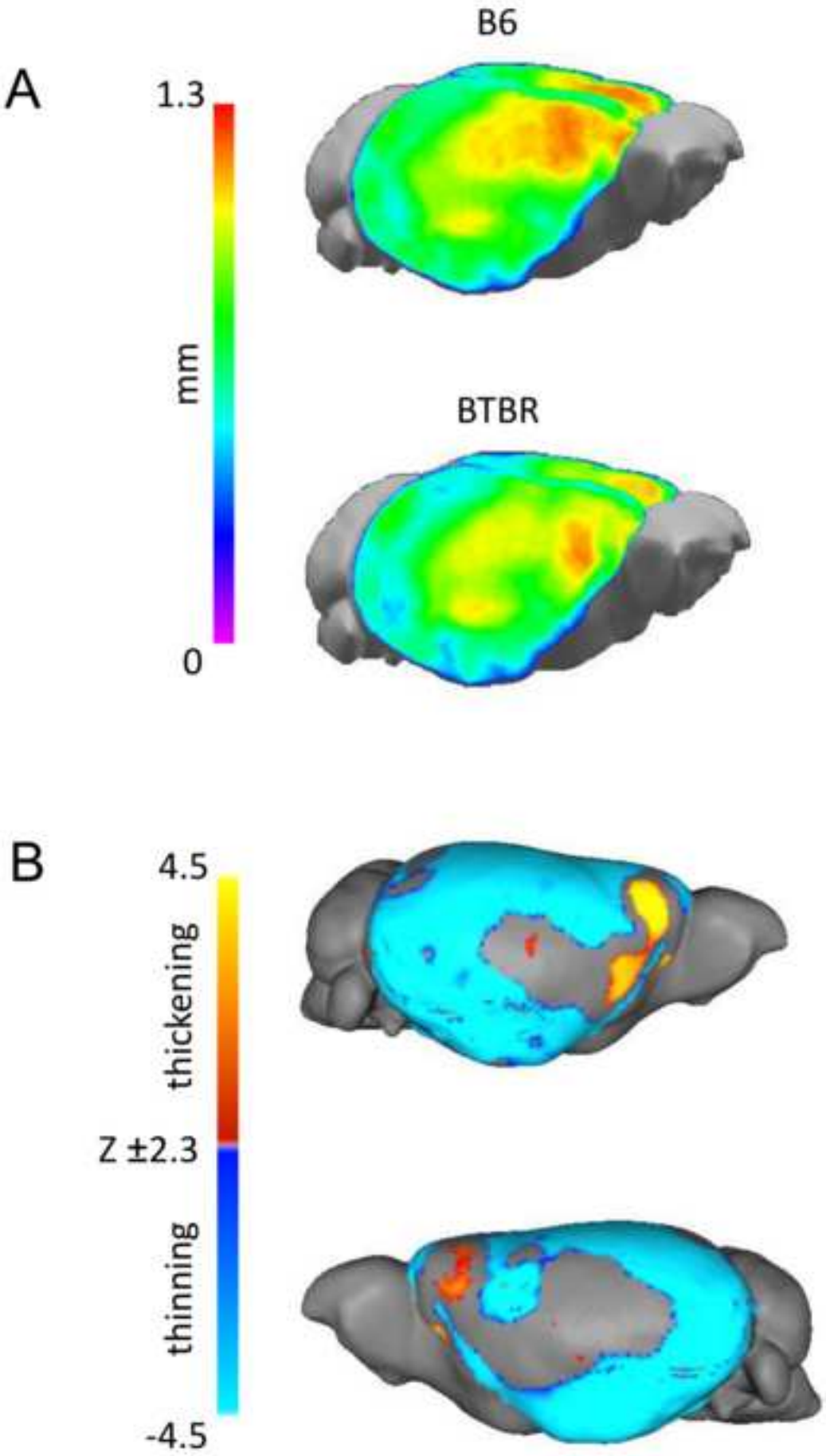

Figure S1

Click here to download high resolution image

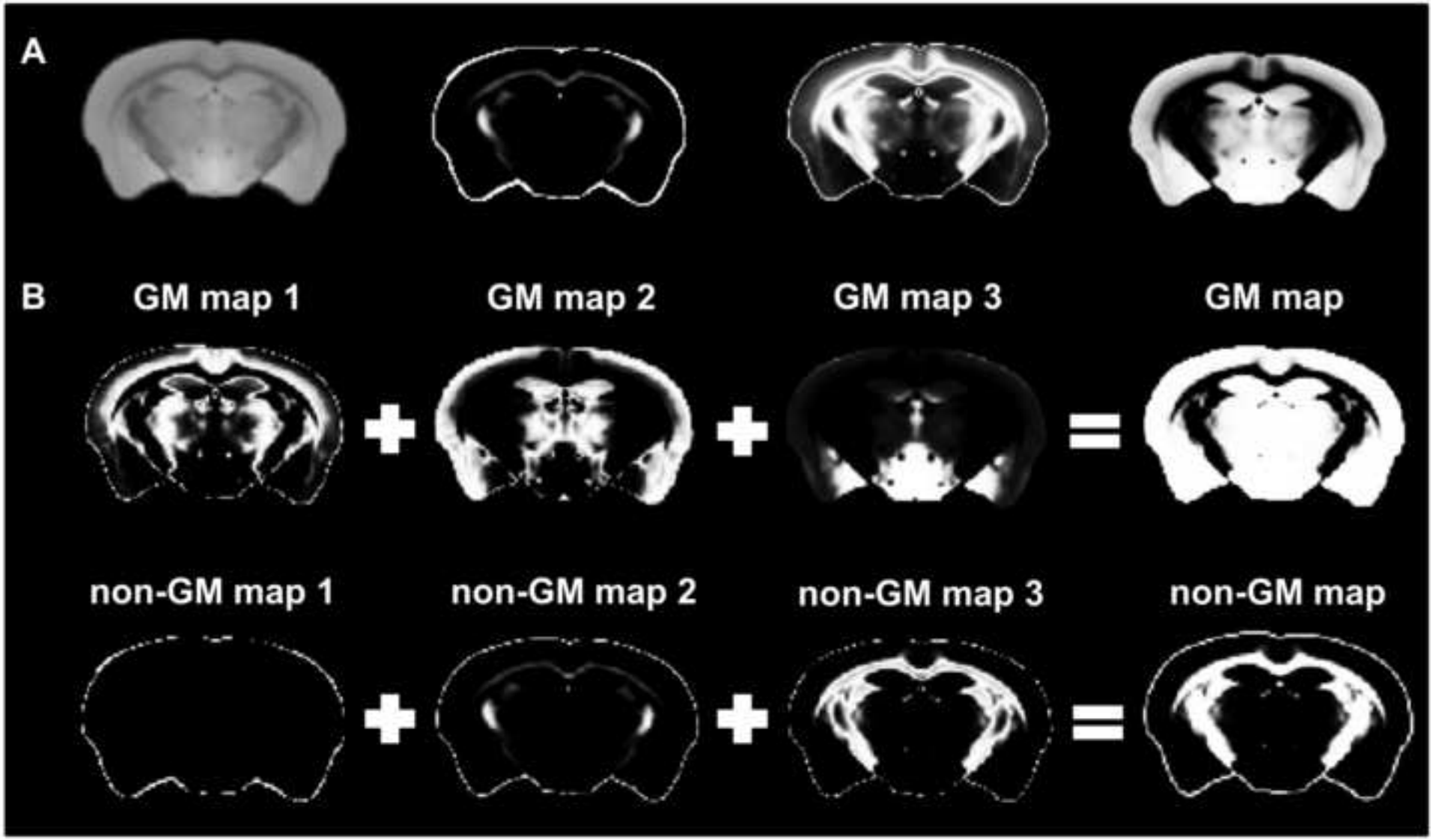

Figure S2

Click here to download high resolution image

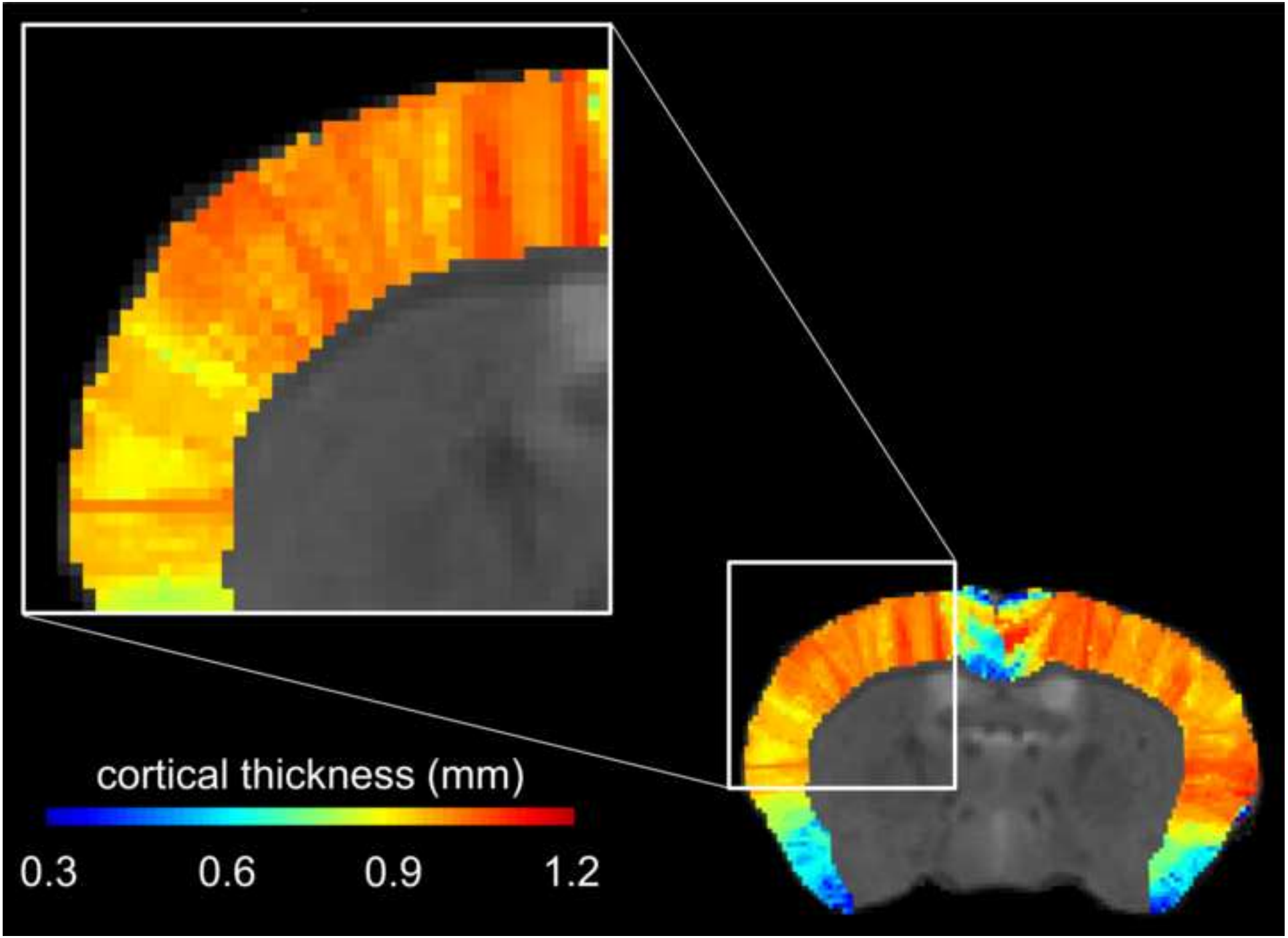

Figure S3

Click here to download high resolution image